





RESEARCH ARTICLE | JUNE 09 2020

Chaos and periodicities in a climatic time series of the Iberian Margin

Berenice Rojo-Garibaldi ; David Alberto Salas-de-León ; María Adela Monreal-Gómez ; Simone Giannerini ; Jlyan H. E. Cartwright 

 Check for updates

Chaos 30, 063126 (2020)

<https://doi.org/10.1063/1.5123509>



View
Online



Export
Citation

CrossMark

Articles You May Be Interested In

Preliminary assessment of aridity conditions in the Iberian Peninsula

AIP Conference Proceedings (June 2016)

Spatial distribution of climate indices in the Iberian Peninsula

AIP Conference Proceedings (March 2015)

Nonoptimal propagation of advertisement calls of midwife toads in Iberian habitats

J Acoust Soc Am (February 2006)

AIP Advances

Why Publish With Us?



25 DAYS
average time
to 1st decision



740+ DOWNLOADS
average per article



INCLUSIVE
scope

[Learn More](#)

Chaos and periodicities in a climatic time series of the Iberian Margin

Cite as: Chaos 30, 063126 (2020); doi: 10.1063/1.5123509

Submitted: 7 August 2019 · Accepted: 6 May 2020 ·

Published Online: 9 June 2020



View Online



Export Citation



CrossMark

Berenice Rojo-Garibaldi,^{1,a}  David Alberto Salas-de-León,²  María Adela Monreal-Cómez,² 
Simone Giannerini,³  and Julyan H. E. Cartwright^{4,5} 

AFFILIATIONS

¹Posgrado en Ciencias del Mar y Limnología, Universidad Nacional Autónoma de México, Av. Universidad 3000, Col. Copilco, Del. Coyoacán, Cd.Mx. 04510, Mexico

²Instituto de Ciencias del Mar y Limnología, Universidad Nacional Autónoma de México, Av. Universidad 3000, Col. Copilco, Del. Coyoacán, Cd.Mx. 04510, Mexico

³Dipartimento di Scienze Statistiche “Paolo Fortunati”, Università di Bologna, Via delle Belle Arti 41, 40126 Bologna, Italy

⁴Instituto Andaluz de Ciencias de la Tierra, CSIC—Universidad de Granada, Armilla, 18100 Granada, Spain

⁵Instituto Carlos I de Física Teórica y Computacional, Universidad de Granada, 18071 Granada, Spain

^aAuthor to whom correspondence should be addressed: bendscuevas@gmail.com

ABSTRACT

We analyze the time series of the temperature of the sedimentary core MD01-2443 originating from the Iberian Margin with a duration of 420 kyr. The series has been tested for unit-root and a long term trend is estimated. We identify four significant periodicities together with a low climatic activity every 100 kyr, and these were associated with internal and external forcings. Also, we identify a high-frequency fast component that acts on top of a nonlinear, irreversible slow-changing dynamics. We find the presence of chaos in the climate of the Iberian Margin by means of a neural network asymptotic test on the largest Lyapunov exponent. The analysis suggests that the chaotic dynamics is associated with the fast high-frequency component. We also carry out a statistical analysis of the dimensionality of the attractor. Our results confirm the possibility that periodic behavior and chaos may coexist on different time scales. This could lead to different degrees of predictability in the climate system according to the characteristic time scales and/or phase-space locations.

Published under license by AIP Publishing. <https://doi.org/10.1063/1.5123509>

The climatic events that occurred throughout the history of our planet leave traces through records that allow us to reconstruct the underlying dynamics and possibly date the most important episodes. Time series analysis helps identifying whether internal or external forcing is involved in climate dynamics. However, most of the research in the area focuses on linear methods or deals with identifying and dating the main events; nonlinear time series analysis is still under-utilized. Our results show the importance of incorporating a proper nonlinear analysis in the subject. We focus on the Iberian Margin, since it has a long temperature record and relatively few studies have been carried out in this area. By using both linear and nonlinear methods, we identify both chaotic and periodic, sawtooth type, behavior and these could be coupled at different time scales. We apply a comprehensive toolset of nonlinear and nonparametric methods, and these include kernel smoothing for non-parametric estimation of the trend and quasi-periodic components, wild-bootstrap methods to

associate a confidence band with the estimated trend, advanced unit-root tests for non-stationarity, entropy based tests for non-linearity, neural networks based tests for chaos. Also, by combining bootstrap methods and the theory of U-statistics, we obtain a proper confidence interval for the correlation dimension. Chaotic dynamics can make slight changes in the Iberian Margin environment cause greater climatic variability in the region. At the same time, the presence of different dynamics over characteristic time scales can reflect on the presence of “windows” of predictability that need to be substantiated.

I. INTRODUCTION

Marine isotope stages (MISs), sometimes termed oxygen isotope stages (OISs), show alternating periods of cold and heat in the Earth’s climate. These stages serve to deduce the temperature and

climate of the world in a certain period of the past using data of the isotopes of oxygen taken from seabed sediment samples. Cores are taken deep enough and large enough to see the different strata in the sedimentary column in the sea floor. Each stage represents a period of the temperature measured in tens of thousands, hundreds of thousands, or even millions of years. A complete study of these isotopic stages reveals the advance and retreat of the ice during the last ice ages and the rises or falls in sea level. Thus, glaciation times and intermediate periods between glaciation can be determined. (These cycles are also recorded in samples of ice and ancient pollen.) An isotopic stage can represent a glacial or interglacial period and also a stadial or interstadial one. A stadial is a cold period during an interglacial, not cold enough to be considered a glacial, and an interstadial is a warm period within a glacial that is not long enough or warm enough to be called an interglacial. These climate variations are attributable to astronomical processes, to variations in the orbit of the Earth, or to changes in the solar radiation. They affect the circulation of the oceans and the distribution of water masses, which store and distribute heat, being, therefore, key to the climate of the Earth.

High-resolution marine sediment cores of the Iberian Margin contain records of the temporal variations of the different water masses, which come from the northern part of the Atlantic and from the Antarctic; these variations of the water masses represent variations in the climate of the Earth. In marine sediment cores, $\delta^{18}\text{O}$ records of benthic foraminifera resemble the Antarctic temperature signal, while the $\delta^{18}\text{O}$ time series of planktonic foraminifera exhibit changes similar to those found in Greenland ice cores.¹⁻⁴ The differences in the isotopic composition between surface and deep waters of the Iberian Margin provide a first independent verification of earlier methane interhemispheric phasing for the last climate cycle,⁵ which makes the Iberian Margin a focal point for the comprehensive assessment of climate variability in both hemispheres over long periods of time.⁴ The sea surface temperature, derived from the sedimentary alkenones in the Iberian Margin, is coupled with the $\delta^{18}\text{O}$ records of *Globigerina bulloides*, which makes this useful as a climate proxy. The specific characteristics of the sedimentation of the Iberian Margin come from the displacement between the ages of alkenones and foraminifera from intervals of identical sediment depth.^{4,6} Thus, time series information obtained from cores of the Iberian Margin is very important to understand the evolution of the Earth's climate during a large part of the Quaternary.

Time series analysis has proven to be a key tool for the study of paleoclimatic data. Alongside the linear approach⁷ and climate modeling, the paradigm of chaos theory and nonlinear dynamics fostered the introduction of new methods and techniques for analyzing complex phenomena. The approach was first investigated within the physics community (see, e.g., Kantz and Schreiber,⁸ Abarbanel,⁹ and references therein) and then revisited and possibly made more rigorous by the mathematics and statistics community (see, e.g., Chan and Tong,¹⁰ Giannerini and Rosa,¹¹ Giannerini,¹² Fan and Yao,¹³ and references therein). It is also worth mentioning the upsurge of interest on climate change within the econometrics community, see, for instance, Hillebrand *et al.*¹⁴ and "climate econometrics."¹⁵

In this study, we analyze the temperature time series obtained from alkenone records in the marine sediment core MD01-2443 of the Iberian Margin, which has a duration of 420 kyr (1 kyr = 1000

years). We study the stationarity of the series by means of appropriate kernel smoothing techniques, wild-bootstrap methods, and unit-root tests. Also, we identify the main (quasi)-periodicities involved in climatic variability by using both wavelets and spectral analysis. The nonlinearity of the series is assessed through a test for irreversibility and an entropy metric bootstrap test. Furthermore, we test for the presence of chaos through a neural networks based asymptotic test on the largest Lyapunov exponent. The results are confirmed through the direct estimation of the largest Lyapunov exponent. Finally, we analyze the fractality of the reconstructed attractor by means of the correlation dimension for which we derive a proper confidence interval based both on asymptotic theory and on bootstrap methods. The results point clearly at the presence of an interplay between chaotic dynamics, possibly acting at a fast time scale, and quasi-periodic oscillators that are associated with the slow dynamics and the main spectral peaks. The analysis of the correlation dimension is not conclusive in that the uncertainty is too high and the estimates do not level off with increasing embedding dimension. The results hint at the presence of two scaling regions and this corroborates the hypothesis of a coupled chaotic system with different time scales.

II. DATA AND METHODS

A. Data pre-processing

For this study, we used alkenone records of the marine sediment core MD01-2443 from 37°52.85'N, 10°10.57'W, at 2925 m below sea level, from Martrat *et al.*⁴ Alkenones are proxies or indicators of the temperature and measure the evolution of the climate during the last 420 kyr. Due to the nature of the data, the original time series is not equally spaced and has been made regular by means of spline interpolation. All the analyses have been put forward through Matlab¹⁶ and R.¹⁷ The reconstructed series is equispaced with an interval of 10 years for an overall sample size of 4194 data points.

B. Estimation of the trend, quasi-periodic behavior, and unit-root tests

One of the first steps of the analysis is to assess the presence of a trend or any other non-stationary component. The presence of a deterministic trend can be tested by means of regression over smooth functions of time. We used recurrence graphs as a heuristic tool to study the stationarity of the series. In physical terms, these compare the distribution of distances between pairs of vectors in the reconstructed state space with the distribution of distances between different orbits evolving over time.¹⁸

We also test for the presence of a stochastic trend, i.e., whether the series is integrated and the observed trend is due a random walk component. Such kind of tests are popular in the econometrics literature and are known as unit-root tests;¹⁹ for more details see the [Appendix](#).

Once the unit-root hypothesis has been ruled out or the series has been differenced, we estimated the trend and the quasi-periodic components of the series by means of a nonparametric kernel

smoothing approach. We assume the following:

$$\begin{aligned} X_t &= m(t/n) + \sigma_t u_t, \\ u_t &= \sum_{j=0}^{\infty} \psi_j \varepsilon_{t-j}, \quad \psi_0 = 1, \end{aligned} \tag{1}$$

where $\{\varepsilon_t\}$ is a zero mean i.i.d. sequence with constant variance and finite fourth moments, $m(\cdot)$ is a smooth deterministic trend function, and u_t is a stationary linear process with σ_t accounting for unconditional heteroskedasticity. We estimate $m(\cdot)$ by means of a local polynomial smoother (loess). For the estimation of the long-run trend, the degree of the smoother has been set to one as to mitigate boundary effects, otherwise the order is two. The confidence bands at level 95% for the nonparametric estimator of the trend have been derived by using an autoregressive wild-bootstrap scheme; for more details on scheme see the [Appendix](#). The scheme provides valid confidence intervals under the assumptions as in Eq. (1), where the detrended series is dependent. For more details, see Friedrich *et al.*²⁰

C. Analysis of the periodic behavior: Wavelet methods and spectral analysis

The periodic behavior of the series has been studied by means of spectral analysis and wavelet methods. Both methods rely on finding a decomposition of the series by means of orthonormal bases of the Hilbert space of square integrable functions. In particular, spectral analysis focuses on the frequency domain as the total energy is decomposed into combination of sinusoids. We used both the raw periodogram and its kernel smoothed version, which is a consistent estimator of the true spectrum.^{13,21} Also, we used the autoregressive spectrum to cross-check the result. Wavelet methods decompose the signal in terms of wavelets that typically are not periodic. This is useful in the presence of non-stationary series^{22,23} and when the time information is important besides the frequency content of the series. For each application, a particular shape or *mother wave*, is chosen; in our case, the Morlet wavelet was used. Many types of individual mother wavelets have oscillations that vary in wavelength; however, Morlet wavelets have a constant wavelength and are popular because the frequency significance of the output is clear.^{24–27}

D. Nonlinearity and chaos

In order to assess the nonlinear nature of the data generating process, we have used a test for time reversibility introduced in Diks *et al.*²⁸ Under the null hypothesis, the process that has generated the observed time series is a nonlinear static transformation of a linear Gaussian random process. We also employed a general test for nonlinear serial dependence introduced in Giannerini *et al.*²⁹ and based upon the combination of a metric entropy (Hellinger distance) and a suitable smoothed sieve bootstrap scheme. The test requires very mild assumptions and leads to asymptotically valid inferences under the null hypothesis that the data generating process admits an infinite autoregressive representation.

Once nonlinearity has been ascertained, we focus on testing for the presence of chaos through the largest Lyapunov exponent that quantifies the so-called initial value sensitivity. Assume that the

series is generated by the following dynamical system in \mathbb{R}^m :

$$X_t = F(X_{t-1}) \quad X_t \in \mathbb{R}^m, \tag{2}$$

and let X_0 and X'_0 be two close initial conditions and X_n and X'_n their value after n time steps, respectively. It results

$$\|X_n - X'_n\| \approx \exp(n \lambda_1) \|X_0 - X'_0\|,$$

where $\|\cdot\|$ is a suitable norm and $\delta = \|X_0 - X'_0\|$ is a small perturbation. Hence,

$$\lambda_1 = \lim_{n \rightarrow \infty} \lim_{\delta \rightarrow 0} \frac{1}{n} \ln \left(\frac{\|X_n - X'_n\|}{\|X_0 - X'_0\|} \right) \tag{3}$$

is the global largest Lyapunov exponent. Note that

$$X_n - X'_n \approx \delta \cdot DF^{(n)}(X_0) = \delta \prod_{t=0}^{M-1} DF(X_t) = \delta \prod_{t=0}^{M-1} J_{M-t},$$

where $F^{(n)}(X_0)$ is the n -fold iteration of the map F and J_t is the Jacobian of the map F evaluated at X_t . Hence, it results

$$\lambda_1 = \lim_{M \rightarrow \infty} \frac{1}{2M} \ln v_1(\mathbf{T}_M^T \mathbf{T}_M), \tag{4}$$

where $\mathbf{T}_M = \prod_{t=0}^{M-1} J_{M-t}$ and $v_1(A)$ is the largest eigenvalue of matrix A . Clearly, λ_1 measures the average rate of divergence of nearby starting trajectories and a chaotic dynamics implies $\lambda_1 > 0$. The two equivalent definitions of the largest Lyapunov exponent given in Eq. (3) and Eq. (4) are reflected in the two approaches to estimating it in finite samples. The first approach refers to Eq. (3) and is called *direct* since it finds close pairs of state vectors and measures the average divergence S of trajectories over time.^{30,31} Then, typically the logarithm of such a divergence S is plotted over time and if it is possible to identify a linear scaling region, then its slope is the direct estimator of λ_1 ; for more details on direct estimators, see the [Appendix](#). In order to verify the reliability of the estimate usually the exercise is replicated for a range of embedding dimensions and time delays. One problem with this approach is that it is sensitive to dynamic noise in that it cannot distinguish between divergence due to noise from exponential divergence due to the chaotic dynamics.¹¹ Moreover, there are no results on the asymptotic distribution of the estimator so that it is not possible to test the hypothesis of chaos. In Giannerini and Rosa,³² a bootstrap solution to the problem is proposed but the intrinsic sensitivity to noise of the direct estimator remains so that we only use it to cross-check the result from the *Jacobian* estimator which is based upon a neural networks model of the map F and its Jacobian J [refer to Eq. (4)]. The modeling step allows us to filter out the effect of noise, obtaining consistent estimators and a proper statistical test for chaos.³³

Another signature of chaotic dynamics is the presence of a fractal attractor. The literature on fractal dimensions is vast and the interested reader is referred to Pesin,³⁴ Cutler³⁵ for a theoretical account. Here, we focus on the correlation dimension, whose use has been popularized in Grassberger and Procaccia³⁶ (see also Cutler³⁷). Let F be a dynamical system over a state space $\mathcal{X} \subseteq \mathbb{R}^m$ equipped

with an invariant measure μ . Then, the correlation integral is defined as

$$C_\mu(\varepsilon) = P_{\mu \otimes \mu}(\|\mathbf{X} - \mathbf{Y}\| \leq \varepsilon), \tag{5}$$

where \mathbf{X} and \mathbf{Y} are independent and distributed according to the measure μ and $I(A)$ is the indicator function over set A . If there exists a constant d_2 such that $C_\mu(\varepsilon) \approx \text{const.} \times \varepsilon^{d_2}$, then

$$d_2 = \lim_{\varepsilon \rightarrow 0} \frac{\log C_\mu(\varepsilon)}{\log \varepsilon} \tag{6}$$

is called the correlation dimension of μ .

The most used estimator for d_2 is derived from the sample version of the correlation integral

$$\hat{C}_\mu(\varepsilon) = \frac{2}{n(n-1)} \sum_{i \neq j} I(\|x_i - x_j\| \leq \varepsilon). \tag{7}$$

Usually, $\log \hat{C}_\mu(\varepsilon)$ is plotted against $\log \varepsilon$ and the slope of the linear scaling region is taken as the estimator of d_2 . For a review of other estimators see Borovkova³⁸ and Cutler.³⁵ As summarized in Chan and Tong (Chap. 5.1),¹⁰ the reliability of the estimators of the fractal dimension has been questioned and depends upon a number of factors such as the lacunarity of the invariant measure, boundary effects, effects due to noise, and filter effects. Moreover, there is no agreement on the sample size needed to obtain a good estimate as the various studies rely on different assumptions. In any case, the assessment of the standard error of the estimates is a mandatory requirement and we implemented both the asymptotic version described in Borovkova³⁹ and Borovkova *et al.*³⁸ and a bootstrap version similar to that of Borovkova *et al.*⁴⁰ Both of them are based on the Hoeffding decomposition of U-statistics.

III. RESULTS

Figure 1, blue line, shows the time plot of the original series (after interpolation), which represents temperature values in Celsius

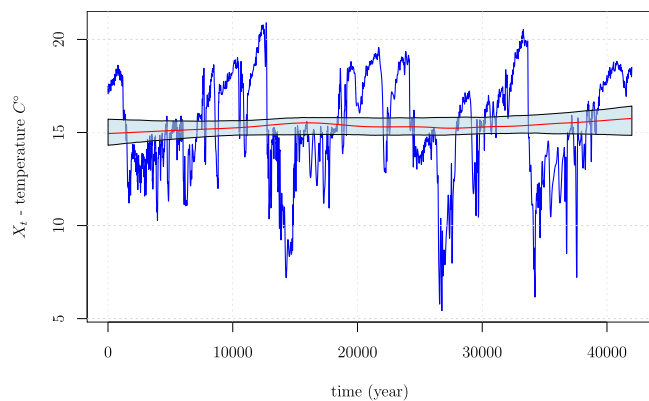


FIG. 1. Temperature time series (in Celsius) for the Iberian Margin, obtained from the proxies of alkenones from the sedimentary core MD01-2443: interpolated original (blue line) and long-run trend (red line), together with confidence bands at 95% (light blue).

ranging from 60 to 420 000 years before the Common Era (BCE). The series has a maximum of 20.91 °C and a minimum of 5.41 °C, an arithmetic mean of 14.71 °C, a standard deviation of 2.76 °C, and a variance of 7.65 °C². The series shows three cooling events, the coldest at approximately 267.63 kyr, while in the case of warming, five events are observed, the highest temperature being at 126.9 kyr approximately. Note that the four earlier warming events are of greater amplitude than the most recent. On the other hand, the temperature trend in the 6 kyr closest to the present is clearly downward. The estimated long-run trend (in red in Fig. 1) seems to indicate some sort of tendency but this is ruled out if we take into account the uncertainty (confidence bands in light blue). Moreover, by applying the three unit-root tests described in Sec. II B, we also rule out the possibility of a random walk behavior. In particular, the test statistic for the test of Chan *et al.*⁴¹ results is 73.56 with a p -value $< 1 \times 10^{-4}$, whereas the statistics for the tests of Ng and Perron⁴² and Perron and Qu⁴³ result are -25.28 and -22.74 , respectively, with a p -value $< 1 \times 10^{-3}$ in both cases. Overall, there is evidence that the process that has generated the Iberian margin time series is stationary so that we can proceed with the analysis by assuming this.

The smoothed spectral density function together with the normalized spectrum are shown in Fig. 2. They present three well-defined peaks, the most important one being at 10.5 kyr, followed by the 4- and 2-kyr ones. There is also a fourth peak at 7 kyr but with less spectral amplitude. These peaks were verified by using the autoregressive spectral density function. The wavelet spectrum obtained by the Morlet method (Fig. 3) shows a greater variability from 60 to 150 kyr. Between 60 and 150 kyr, one can see an oscillation that begins with a period between 0.5 and 2 kyr, which goes

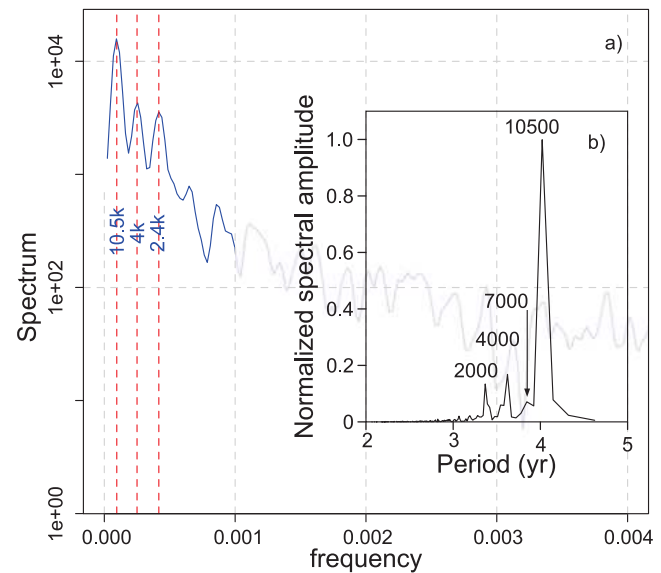


FIG. 2. (a) Smoothed spectral density function for the Iberian margin time series. The three dominant peaks are indicated with dashed lines together with their associated period (in blue). (b) Normalized spectrum from the same series. The same peaks are observed as in the density function, with an additional peak at 7000 yr.

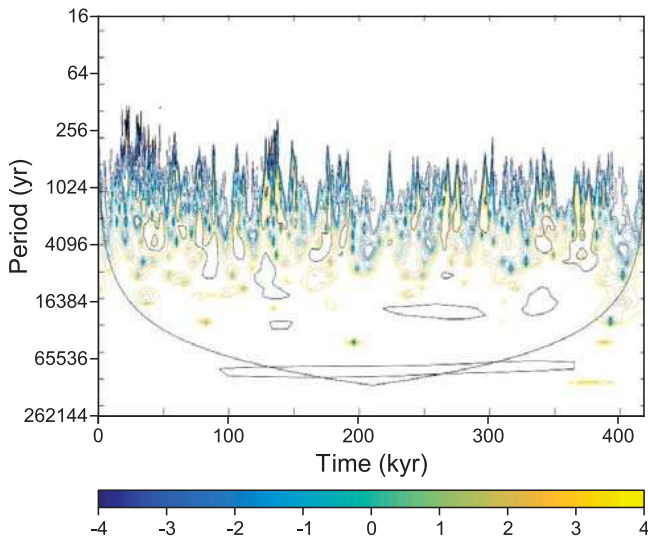


FIG. 3. Wavelet spectrum (Morlet) for the Iberian Margin time series. The color bar is the variance, and the lower black line represents the cone of influence; anything below is dubious.

on until having a period between 3 and 8 kyr. This repeats approximately from 160 to 180 kyr, between 240 to 300 kyr and 330 to 380 kyr, although in the last interval, it begins with larger periods and evolves toward shorter periods. The lag between these three time intervals are 60 and 30 kyr, respectively, which are multiples of 10 kyr. On the other hand, it is interesting to note the low activity that is seen at approximately 100, 200, 280, and 400 kyr; this represents a process of low climatic activity every 100 kyr.

It is not difficult to appreciate from Fig. 1 that the shape of the series is of a Fourier sawtooth type that can be modeled by using the dominant periodicities as follows:

$$T(t) = \left| \frac{A}{2} + \frac{A}{2\pi} \sum_{n=-\infty}^{\infty} \frac{1}{n} \exp \left\{ j \left(n\omega_0 t + \frac{\pi}{2} \right) \right\} \right|, \quad (8)$$

where $\omega = 2\pi/T$ is the angular frequency. We take $n = 1$ and expand for eight harmonics as to obtain an approximate model of the long-run periodicity of the temperature (Fig. 4, black line). The model follows the general trend of the evolution of temperature but fails to capture the quasi-periodic behavior that could be also ascribed to a stochastic forcing factor. Hence, in order to extract the long term periodic component, we used the local quadratic smoother defined in Sec. II B with a time span that approximately matches the duration of the cooling cycle (7 kyr). The results are shown in Fig. 4, blue line. In Fig. 5, we present the time series together with the estimated low-frequency trend cycle (red line, left axis) where the time span is 1 kyr. The blue line represents the residual high-frequency or fast dynamics (blue line, right axis). From Figs. 4 and 5, it can be seen that the warming periods are characterized by a slow increase followed by a fast decrease toward the three main cooling events. These present greater variability with respect to warm ones that, on the other hand, are characterized by oscillations

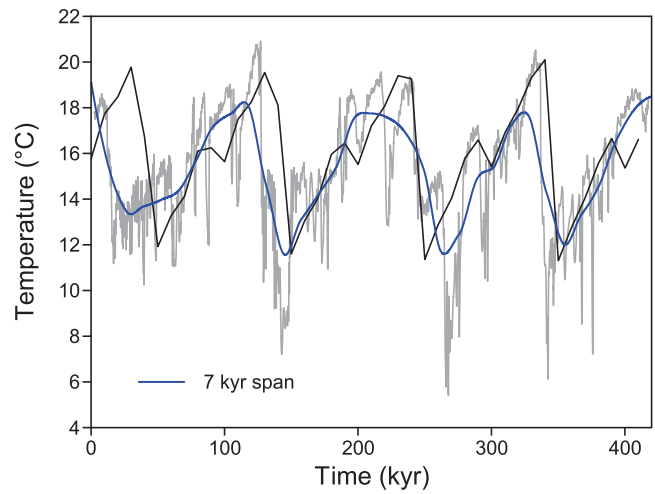


FIG. 4. Temperature behavior from 420 kyr to 60 yr BCE. Results of the model (black line) and original temperature time series (grey line) together with the estimated long-run cycle-trend (blue line).

that are more persistent and larger in amplitude, and this could indicate greater climatic stability during warm periods. This asymmetric behavior hints at the presence of a nonlinear irreversible oscillator.

The frequency distribution is tri-modal, with the maxima of the two major peaks at 14.32°C and at 18.34°C, and a third at 6.89°C; these represent the dominant temperatures during the cold and warm periods, respectively (Fig. 6).

The first and second derivatives of the temperature time series (Fig. 7) show important events at 140 kyr, with a duration of approximately 50 kyr, and a period of high variability from 50 kyr to

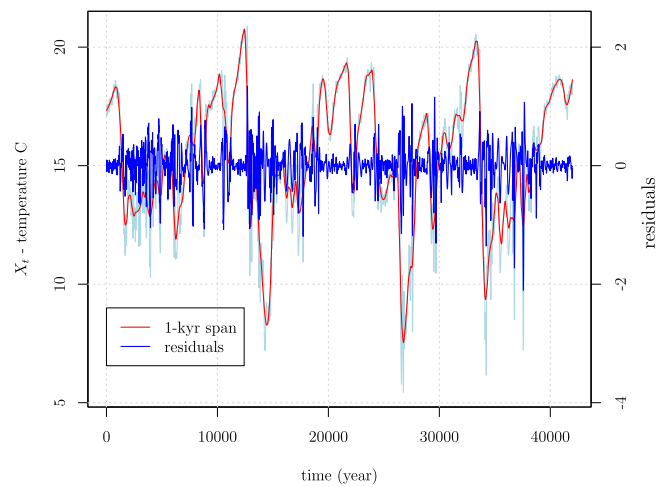


FIG. 5. Temperature time series (light blue) together with the low-frequency cycle-trend (red line, 1 kyr span, left axis) and the residual high-frequency component (blue line, right axis).

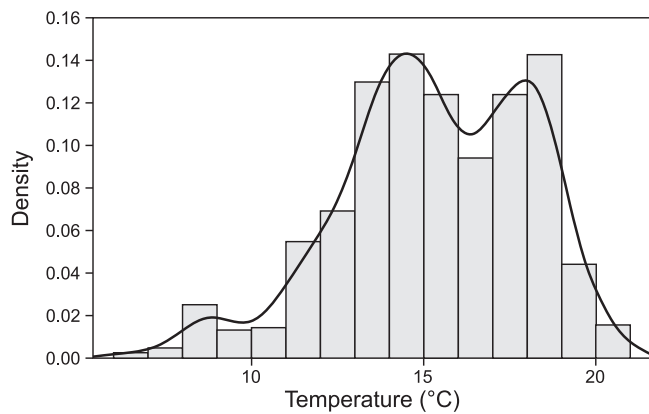


FIG. 6. Histogram of the of temperature of the time series obtained from the proxies of alkenones from the sedimentary core MD01-2443 with the Freedman–Diaconis technique. The black line denotes a kernel density estimate.

approximately the present with a relatively low variability at 30 kyr. It is worth noting that these events coincide with the high variability observed during the periods prior to the cold periods. Also, the evolution toward the cold stages occurs in a relatively smooth way with gradient that on average is 1.44×10^{-4} (because the slope is very small, the angle is almost the same, 1.45×10^{-4}). The change between a cold period (average slope of 2.55×10^{-3}) and a warm one is 1.77×10^{-1} higher; this may be due to the phase change between water and ice and the latent heat of melting of ice. When ice forms (melts), energy is released into (absorbed from) the environment; this causes the temperature in the cooling (heating) curves of water

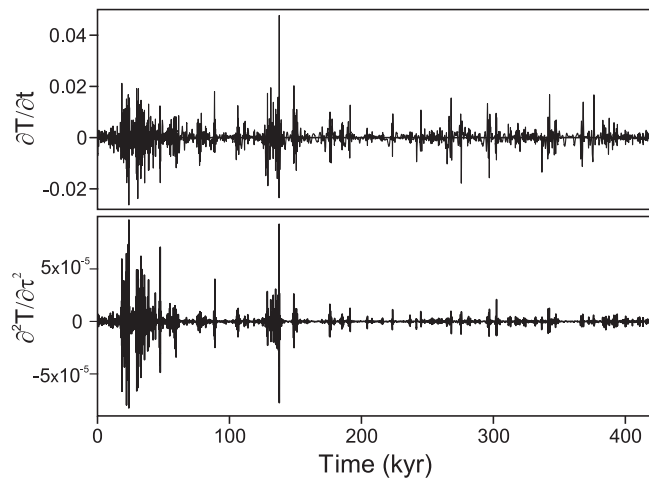


FIG. 7. Upper panel: first derivative of the temperature and lower panel: second derivative. The first and second derivatives serve to identify the main heating events; the second is capable of distinguishing between events of varying magnitude and incorporates information about conditions before and after an abrupt event.

to stall and show a plateau effect until the production (melting) of ice has stopped. Thus, cold stage events involving this phase transition are slow compared to warm stage events without any such phase transition. The change in temperature between the stages of approximately 100 kyr, centered on the intermediate time of the stage, suggest the presence of a sinusoidal period of 420 kyr. Of course, this conjecture can only be verified with a longer time series. The empirical autocorrelation function presents a strong persistence which resembles that of continuous-time processes and does not fade away as the lag increases. The partial correlogram presents a large positive value at lag 1 and a negative value at lag 2 and hints at the presence of moving average components where the dynamic noise enters into the equation of motion. This will be further discussed below.

A. Nonlinearity and chaos

As a first step, we test for irreversibility and nonlinearity by using the two tests described in Sec. II D. The value of the test statistic for irreversibility results $Q = 0.002$ with a p -value of 0.001; this was obtained with a bandwidth of 0.2 and by applying the block method with a value of 30 blocks. The results of the entropy test for nonlinearity of Giannerini *et al.*²⁹ are shown in Fig. 8. The measure S_k can be interpreted as a nonlinear autocorrelation function at lag k where the confidence bands represent the null hypothesis of linearity at 99% (green) and 99.9% (blue). Here, the number of smoothed sieve bootstrap replicates was set to $B = 1000$, and we chose the reference bandwidth method for kernel density estimation. Also, in order to cope with the slow decay of the ACF, we have set the max order of the autoregressive sieve to 1000. Even in this conservative setting, the null hypothesis of linearity is clearly rejected and we observe a nonlinear significant effect from 5 to 7 kyr.

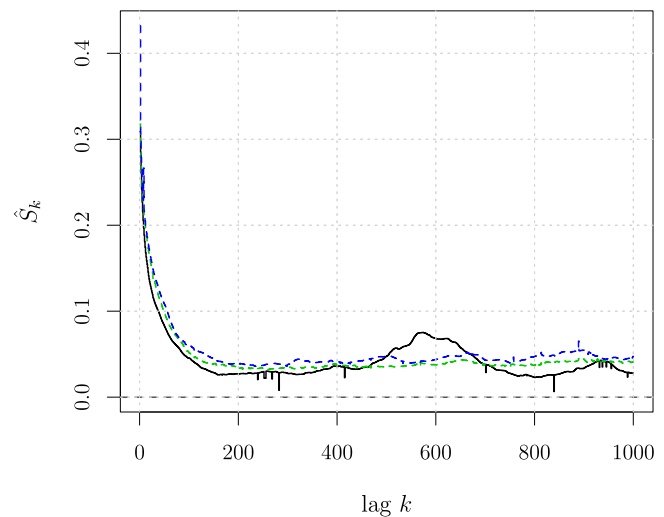


FIG. 8. Entropy measure S_k computed on the Iberian margin time series up to 1000 lags (10 kyr). The confidence bands at 99% (green) and 99.9% (blue) correspond to the null hypothesis of linearity.

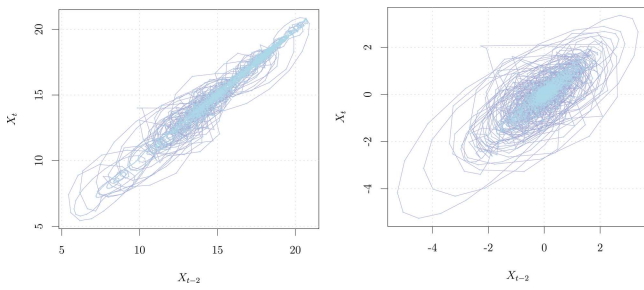


FIG. 9. Phase-space diagram for the temperature time series of the Iberian Margin with $\tau = 2$. Left panel: original time series; right panel: high-frequency component (see Fig. 6).

The results point at the existence of an irreversible nonlinear process behind the Iberian Margin time series. This is in agreement with the fact that climate behavior is known to be associated with Milankovitch Cycles, which in turn are related to solar cycles that are also irreversible.^{28,44} It is feasible to think that a nonlinear process (solar cycles) is generating a change in the temperature (Iberian Margin), causing the behavior of this change to be nonlinear as well.

In order to obtain the attractor reconstruction, the time delay τ and the embedding dimension d were derived in first place by using heuristic methods based on the average mutual information and on false nearest neighbors (see the Appendix). In particular, these indicate that a time delay $\tau = 1$ or 2 is sufficient and that the embedding dimension should be at least 6 but the results are very sensitive upon the settings used. In Fig. 9, we show the phase-space portraits of the reconstructed series with $\tau = 2$. The left panel shows the original series, whereas the right panel shows its high-frequency fast components. The behavior of the attractor together with that observed in Fig. 6 can be associated with the great variability that is generated during cold events, producing a system whose dynamic behavior is mostly rapid, since after a major event, the rest of the system is characterized by variability in high frequencies.

As also shown in Chan and Tong¹⁰ and Giannerini and Rosa,¹¹ the time delay embedding exercise can be seen as a statistical problem of subset selection within nonparametric modeling. Hence, a consistent model selection criterion will lead to choosing optimal reconstruction parameters and this is the approach we adopted. Also, note that different objectives may require different optimal reconstruction parameters and a reliable result should be robust with respect to reasonable variations of the time delay and embedding dimension.

We test for the presence of chaos through the largest Lyapunov exponent λ_1 as described in Shintani and Linton;³³ the null hypothesis results $H_0 : \lambda_1 \leq 0$ vs $H_1 : \lambda_1 > 0$. As explained in Sec. II D, the Jacobian estimator of λ_1 relies upon a single-hidden-layer neural network of the map and its derivative and the most difficult aspect is training/estimating a network which reaches the global optimum of the target function. We chose the best model by means of the generalized Bayesian Information Criterion (BIC) upon the following grid of parameters:

Parameter	Grid	
Embedding dimension	d	2–16
Time delay	τ	1–10
Number of hidden units	k	1–20

After the first grid search, the model that minimized the BIC was refined and the convergence to the global minimum of the target function was ensured. The results are presented in Table I, first row. The global minimum is reached for embedding dimension $d = 10$ and time delay $\tau = 1$. The estimated Lyapunov exponent $\hat{\lambda}_1 = 0.112$ is significantly positive as the null hypothesis is rejected with a p -value $< 2.2 \times 10^{-16}$. The table also reports the number of hidden units of the network k , the value of the minimized BIC, the asymptotic standard error of $\hat{\lambda}_1$, and the value of the test statistic.

We have repeated the analysis on the high-frequency fast component of Fig. 5. The results, presented in row 2 of Table I, are very similar to those for the original time series. Hence, it seems that the observed chaotic dynamics can be ascribed to the fast time scale high-frequency component of the series that is possibly coupled with an oscillator that acts at slower time scales and is responsible for the observed periodicities. The results for the direct estimator of the Lyapunov exponent are presented in Fig. 10 that shows the plot of $S(t, \varepsilon)$ vs time t [see Eq. (A2)]. The left panel refers to the original series and each curve corresponds to a different embedding dimension d ranging from 10 to 14. The time delay is $\tau = 1$ and $\varepsilon = \sigma/6$, where σ is the standard deviation of the series. The regions where the fit has been computed for each d are highlighted in blue and the average Lyapunov exponent over d results $\hat{\lambda}_1 = 0.148$. The right panel shows same analysis performed over the high-frequency fast component of the series, where $d = 9, \dots, 12$, $\tau = 2$, and $\varepsilon = \sigma/2$. The average Lyapunov exponent over d results $\hat{\lambda}_1 = 0.092$. The two results match approximately those of the Jacobian estimator. However, as mentioned before, we found the results to be very sensitive with respect to the choice of d and, to a lesser extent, τ so that without the guidance of the Jacobian estimator it would have been impossible to come to a definite conclusion. Indeed, note that the curves show two approximately linear scaling regions and without further investigations it would not be possible to pick up the right one. In any case, the information deriving from these curves is still

TABLE I. Output from the best neural network fit from the grid search and test for chaos of the time series of the Iberian Margin (row 1) and the time series of the high-frequency fast component of Fig. 5 (row 2). The table reports the embedding dimension d , the time delay τ , the number of hidden units k , the value of the minimized BIC, the estimated Lyapunov exponent $\hat{\lambda}_1$ together with its asymptotic standard error, the value of the test statistic, and the p -value of the test.

	d	τ	k	BIC	$\hat{\lambda}_1$	Std error	Test	p -value
1.	10	1	16	-15357.36	0.112	0.010	11.72	$< 2.2 \times 10^{-16}$
2.	13	1	12	-16280.13	0.102	0.009	10.77	$< 2.2 \times 10^{-16}$

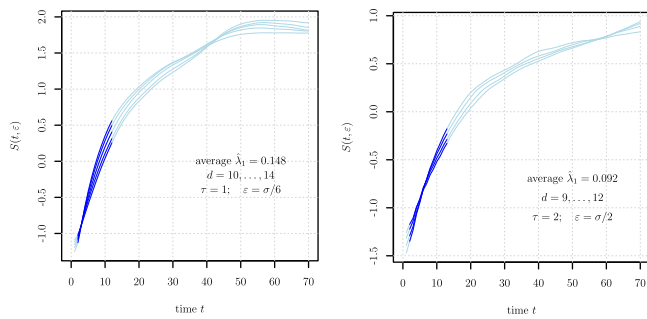


FIG. 10. Average log-divergence $S(t, \varepsilon)$ vs time t [see Eq. (A2)] for the original series (left) and for its high-frequency component (Fig. 5). The regions where the fit has been computed for each d are highlighted in blue, and the average Lyapunov exponent over d is reported.

valuable as it hints at the presence of coupled dynamics with different time scales. Such a behavior could also be due to the presence of noise and will be briefly discussed in the following.

The recurrence plot is presented in Fig. 11; the points show a general tendency to be close to the diagonal and, at the same time, exhibit a coherent structure. This corroborates the hypothesis of a deterministic, possibly chaotic process.

The dimensionality of the attractor has been investigated by means of the correlation dimension computed through the Grassberger and Procaccia estimator.^{36,45} In these computations, the time delay $\tau = 2$ and the Theiler W window, which was calculated with the help of the space-time separation plot, resulted $W = 170$. For each embedding dimension d ranging from 2 to 15 a linear scaling

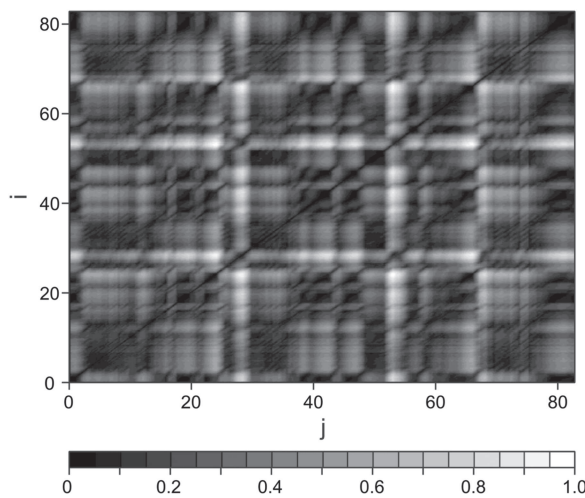


FIG. 11. Recurrence plot: the x -axis is equivalent to j and the y -axis is equivalent to i , which are the index numbers of the data points of the time series. The scale bar on the right side indicates remote color mapping, where white represents a distance zero and black a greater distance. The central diagonal indicates the time when $i = j$.

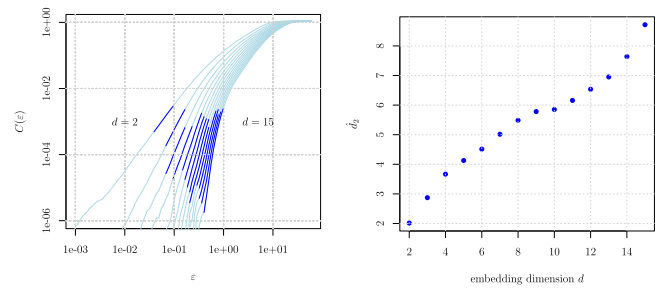


FIG. 12. (left) Correlation integral $C(\varepsilon)$ for the Iberian Margin as a function of ε in the logarithmic scale. The embedding dimension d ranges from 2 to 15 and the optimal linear scaling region upon which the slope is computed is highlighted in blue. (right) estimates of the correlation dimension \hat{d}_2 as a function of the embedding dimension d .

region that maximizes the goodness-of-fit is identified. The scaling regions are highlighted in blue in the left panel of Fig. 12 and their slope is taken as the estimate of the correlation dimension. These are shown in the right panel of Fig. 12. Clearly, the estimates increase with d and do not stabilize. The standard errors also increase with d and are of the order of 0.8 and this makes it impossible to draw a definite conclusion on the dimensionality of the attractor. Note that the log-correlation integral of Fig. 12 shows two linear scaling regions and we asked ourselves whether the true scaling region for $C(\varepsilon)$ could range from 0.01 to 0.2. This is investigated in Fig. 13, where the left panel shows a zoom of Fig. 12 on the region [0.01 – 1] for the correlation integral and the optimal fitting regions are highlighted in blue. The results are shown in the right panel. Also in this case, the estimates for d_2 grow with d without stabilizing. For instance, if we consider $d = 12$, we get $\hat{d}_2 = 2.11$ with an asymptotic standard error of 0.27 and a bootstrap standard error of 0.23. Hence, a 95% confidence interval for d_2 results [1.58, 2.64]. Again, it is not possible to draw conclusions about the fractal nature of the reconstructed attractor. On the one hand, it is true that the estimates of the correlation dimension do increase at a slower rate than d and this suggests the presence of a low-dimensional attractor; on the other

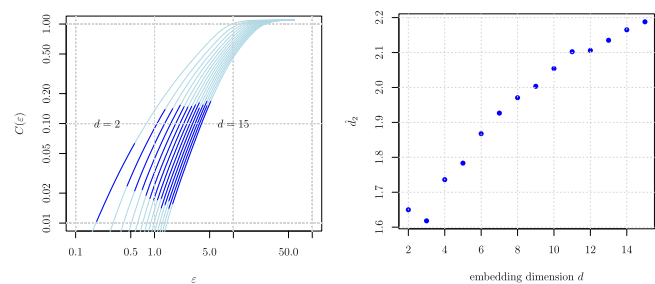


FIG. 13. (left) Correlation integral $C(\varepsilon)$ for the Iberian Margin as a function of ε in the range [0.1, 50] in the logarithmic scale. The embedding dimension d ranges from 2 to 15 and the optimal linear scaling region upon which the slope is computed is highlighted in blue. (right) estimates of the correlation dimension \hat{d}_2 as a function of the embedding dimension d .

hand, it is not possible to draw reliable conclusions on the actual value of d_2 and further investigations are needed.

IV. DISCUSSION

From a visual inspection to the time series spanning MIS 11 and from the results shown by spectral analysis, we see a marked change in climate during the Quaternary, in which the changes from cold to warm temperatures are more abrupt. This type of behavior has already been reported by different authors and is attributed, in most cases, to astronomical forcing.^{4,46–51} Beyond astronomical effects, these episodes do not appear as periodic and are interrupted by excursions away from these cold or warm phases. Nicolis and Nicolis⁴⁶ obtain an attractor whose shape is very similar to that obtained in this study. The winding direction that our attractor takes is apparently always the same. This may indicate that this climatic attractor belongs to a family of attractors that exhibit spiral and screw chaos.⁵² Different studies on climatic attractors,^{46,53–57} find low dimensionality in atmospheric climate time series, one exception being Grassberger⁵⁴ that suggested that the weather had no attractor and also warned that small spurious estimates of the dimension might be obtained if the sample size is not sufficient, or the data are sampled too finely and too smoothed. Petkov *et al.*⁵⁸ and Badin and Domeisen,⁵⁹ found dimensions for their attractor between three and six, working with time series from the Arctic ozone column in the first case and with different stratospheric areas of the northern hemisphere in the second. Zeng *et al.*⁵² pointed out that none of the aforementioned studies fulfill the requirement of Ruelle,⁶⁰ which stipulates that at least $10^{d_2/2}$ data points are necessary for a reliable estimate of dimension d_2 . Moreover, Tsonis *et al.*⁶¹ suggest that about $10^{2+0.4d_2}$ data points are needed for a reliable estimate of the fractal dimension d_2 . Even if the length of our series fulfills both criteria we found that it is not possible to obtain a reliable estimate of the (fractal) dimension of the attractor. This can be due to several factors and will be the subject of future investigations. We argue that similar problems affect most of the studies where a fractal dimension is reported and it is our opinion that an estimate without a proper measure of uncertainty should be reconsidered after a valid confidence interval has been derived. The similarity between our results and those of Nicolis and Nicolis⁴⁶ can indicate the existence of a climatic attractor at the latitudes studied, regardless of the longitude, since both studies were carried out in latitudinally similar regions and, more importantly, using different proxies ($\delta^{18}\text{O}^{46}$). Based on the above, we can conjecture that the Iberian Margin has a climatic attractor of (possibly) low dimensionality, with a deterministic chaotic dynamics.

As for the largest Lyapunov exponent, the correlation integral also presents two scaling regions. As pointed out in Chan and Tong (Chap. 5.1.7),¹⁰ this can be due to the presence of noise and the scaling law for $\varepsilon < \sigma$, where σ is the standard deviation of the noise, only reflects the scaling of the noise. Moreover, there are examples of deterministic systems with dynamic noise where the estimates of d_2 do not level off with d . Another possibility is that there are coupled dynamics with different time scales and the faster dynamics acts as disturbance. This interesting scenario requires further investigations, in any case, note that the BIC criterion selects an embedding dimension of 10, which also results as the dimension where the two

scaling regions become apparent and this can be ascribed to such a phenomenon.

Returning to the results of the spectral analysis, the warm periods show greater climatic stability, which agrees with Martrat *et al.*⁴ who observed that the stable warm periods similar to the Holocene were maintained and although the oscillations were rare, they were generally more pronounced than during ice ages. The highest temperature peak (20.91 °C) in the record was at 126.9 kyr, which is within MIS 5e, the interglacial period from 118 to 130 kyr BCE,^{62,63} while the lowest temperature (5.41 °C) was found at 267.63 kyr, which is included within MIS 8, the cold period from 240 to 300 thousand years ago. Until now, we have found temperatures concordant with the mentioned Marine Isotope Stages. Similarly, we can see that there is a greater warming during MIS 11 than during the Holocene, as suggested by the data from the Labrador Sea of Aksu *et al.*⁶⁴ and Abreu *et al.*⁶⁵ We can also note the similarity of the insolation geometry between these two stages; MIS 11 is often considered the interglacial period analogous to the Holocene because the orbital parameters of the Earth's orbit were very similar to today's.^{26,65,66} However, the most significant warming took place during MIS 5e, very close to one of the last two deglaciations, Termination II, located in SPECMAP at 128 kyr.^{63,67} Our results are in agreement with what was reported by Abreu *et al.*,⁶⁵ who reported MIS 5e as the warmest period for the same study region.

The value shown by the second derivative (140 kyr) coincides with the beginning of Termination II. This, if we rely on the reports of Lorius *et al.*,⁶⁸ who located the midpoint of the warming in Antarctica very close to 140 kyr, is the same value reported in the Devil's Hole geothermal pool (Nevada, USA) oxygen isotope record.^{69–71} Termination II was a time of rapid climate change, when ice sheets melted and sea level rose, as did atmospheric CO₂ concentrations.^{51,72} In the case of the Iberian Margin, Drysdale *et al.*⁷³ put the beginning of Termination II, based on the change of benthic $\delta^{18}\text{O}$ to interglacial values, at 141 ± 2.5 kyr, which places our result within this event. The values obtained in our analysis agree with both dates provided for Termination II, which is to be expected since the sediments of the Iberian Margin preserve an excellent multiproxy paleoclimatic record of Termination II and the last interglacial.^{4,73–78} Undoubtedly, this deglaciation had an important influence on the climatic variation within the Iberian Margin, since its records allow us to identify clearly such events. Through wavelet analysis, low climate variability was observed approximately every 100 kyr. Clearly, the influence of the cycle of eccentricity of the Earth's orbit (100 kyr) can be appreciated, which is to be expected since the late Pleistocene climatic records are dominated by this cyclical behavior.^{63,79,80} It is worth noting that the oscillations occurred during MIS 2–4, MIS 6, MIS 8, and between MIS 9 and 10, which places our oscillations in cold periods, with the exception of MIS 9. In agreement with what has been mentioned above, warm periods have greater climatic stability. We may speculate that perhaps during the MIS 9 there was some important regional disturbance that destabilized the system.

In order to study the nature of suborbital variability within MIS 5 more closely, Oppo *et al.*⁸¹ estimated the power spectra of site 1059 (32 °N, 75 °W, 2985 m, near southern California) with records of $\delta^{18}\text{O}$ of *G. ruber* using the multi-taper method.⁸² The spectral

peak occurs in a wideband between 4.8 and 12 kyr (with peaks of greater power in 6 and 10 kyr). Keigwin and Jones⁸³ found these same periods for the same region but in MIS 3. In our Fourier analysis, periodicities of 4, 7, and 10 kyr were found, and in the wavelet analysis, a band of 3–8 kyr was also obtained, which is very close to the values reported by these authors. What is relevant here is to think that one or two important events should have occurred, with a periodicity of ~ 7 and 10 kyr, which affected not only MIS 3 and 5, but the whole record of 420 kyr (up to MIS 11) and that our record covers all this time and we continue to find these periodicities. We can say that the event should have been large, since these two regions are very far apart from each other.

The 2000-year period found in both Fourier and wavelet analyses recalls the well-known rapid climatic oscillations ranging from 1 to 3 kyr that have been described in the glacial records of Greenland ice cores.^{84–87} These are the Dansgaard–Oeschger cycles (D–O) and the Heinrich events (HE), which are related to Bond cycles.^{47,88,89} Heinrich events are episodes of massive ice discharges in the North Atlantic that are repeated every ~ 5 –10 kyr. Given that the D–O events occurred during the last glacial period and in our wavelet record, we have a period band of 0.5 to 2 kyr between 60 and 150 kyr, covering this period, we can say that these oscillations are likely due to these events. Similarly, if we take into account that, according to our results, these oscillations for the same time interval are crossed to a periodic band of 3 to 8 kyr, we also have the HE as the cause of these oscillations within the interval from 60 to 150 kyr. This leads us to consider two aspects: (1) these events (DO and HE) were the most important ones to be recorded in the Iberian Margin, in such a way that any other event that happened periodically was of lower energy and it is not possible to distinguish it with the methods used, and (2) it is clear, as already mentioned above, that there must have been at least three important events in ~ 2 , 7, and 10 kyr that affected not only the Iberian Margin but the entire northern part of the Atlantic Ocean.

The asymmetric, sawtooth-like behavior that we found is a clear pattern previously noted by Bond *et al.*,⁴⁷ who associated sawtooth-shaped cooling cycles with records of sea surface temperature and atmospheric temperature, maintaining a close relationship to the HE and massive collapse of the Laurentian Ice Sheet. Bond found this pattern in ice core records, and in our case, it is in sedimentary records; however, as we have already mentioned, the Iberian Margin provides records of both the North Atlantic and Antarctic water masses. In addition, according to Bond *et al.*,⁴⁷ this series of heating and cooling cycles is so notorious in the records of the surface of the sea and the atmosphere of the North Atlantic that it must be imprinted in other records of the last glaciation. Hence, we can say that our record also carries information about these cycles and it is very likely that the form of our time series is also due to the HE and to the massive collapses of the Laurentian ice Sheet; only that in our case, it is appreciated beyond the last glacial period. This type of behavior was also observed by Alexandrov *et al.*⁹⁰ in a stochastic analysis carried out through a model to study the climatic variations of the Quaternary; its analysis shows a climatic auto-fluctuation of the sawtooth type close to 100 kyr. This is a peculiar feature of the climatic variability of the Quaternary.

The observed interplay of chaotic and periodic behavior hints at complex interactions between internal and external forcing that

regulate the climate. Since our approach is not based upon a parametric model it is not possible to perform a bifurcation analysis. In Weertman⁹¹ and in Alexandrov *et al.*,^{90,92} the authors were able to observe a climate transition between periodic behavior and chaos. In particular, Weertman,⁹¹ by changing the parameters of the model within a physically acceptable range, marked a difference between a glacial and an interglacial regime and found that a slight change in the parameters produced a climatic switching. Similarly, Alexandrov *et al.*⁹³ by using the model of Saltzman *et al.*^{94–97} identified the different types of change by varying the level of additive noise (using the mean temperature of the ocean) and parametric noise (which represents physical mechanisms that govern the dynamics of the weather). With the variations in these two types of noise, they observe how their system progresses from a transition between small amplitude oscillations to large amplitude oscillations. Remarkably, they find chaotic behavior when increasing the intensity of the noise. Moreover, Alexandrov *et al.*^{90,92} by applying a Saltzman–Sutera model,⁹⁸ found that when the climatic system approaches its bifurcation point, stochastic oscillations of small and large amplitude are generated; that is, smaller noise leads to a transition from order to chaos. In this respect, our results are in agreement with previous studies and confirm the possibility that periodic behavior and chaos can coexist at different time scales.

V. CONCLUSIONS

The results obtained with the Lyapunov exponent indicate that the climatic behavior of the Iberian Margin is chaotic. Note that, as shown in Smith *et al.*⁹⁹ since global Lyapunov exponents are defined in the double limit of infinitesimal perturbations and infinite step-ahead in the future, they cannot pose a practical limit to predictability of the system, whose quantification is an interesting problem that we will address in future investigations. Indeed, nonlinearity implies state-dependent predictability that could call for a different approach. Moreover, due to the presence of different characteristic time scales, the system could be predictable on longer horizons while remaining substantially less predictable on the short term [see also Cencini *et al.* (Chap. 9.4)¹⁰⁰ and Chan and Tong (Chap. 6)¹⁰ for a discussion].

The temperature records present a quasi-periodic sawtooth shape, which is characteristic of oceanic and atmospheric temperature changes. It is through the identification of this pattern that it is possible to associate the chaotic behavior found through the Lyapunov exponent with sudden changes in temperature. Slight changes in the environment of this region could cause greater climatic variability. It was possible to identify the 100 kyr forcing characteristic of the late Pleistocene along with other periodicities (2, 4, 7, and 10 kyr) that we can associate with internal and external forcing and that indicate that prediction over those time scales is feasible. It is the internal forcing or the high-frequency components that are probably causing chaos in the system and the actual predictability of the system can reflect this. In the Iberian Margin climate system, chaos and periodic behavior do not exclude each other. Rather, they coexist as processes with different time scales as a result of the complex interaction between the subsystems that make up the climate.

ACKNOWLEDGMENTS

Berenice Rojo-Garibaldi is grateful for the CONACYT scholarship that supported her study at the Posgrado en Ciencias del Mar y Limnología, Universidad Nacional Autónoma de México.

APPENDIX: FURTHER DETAILS ON TIME SERIES METHODS

1. Unit-root test

Typically, it is assumed that the series X_t , $t = 1, \dots, n$ admits the following decomposition:

$$X_t = m(t) + \phi X_{t-1} + \sigma_t u_t, \quad (A1)$$

where $m(t)$ is a deterministic trend, σ_t is a deterministic sequence, and u_t is a stationary process with zero mean and unit variance. The hypothesis tested is $H_0 : \phi = 1$ against $H_1 : \phi \neq 1$. One of the main problems with unit-root tests such as the popular augmented Dickey-Fuller test is that they break down when σ_t is not constant or u_t is nonlinear. A test suited to deal with this situation has been introduced in Chan *et al.*⁴¹ and it is used here. We also use the tests introduced in Ng and Perron^{42,43} that suffer less from the aforementioned issues.

2. Autoregressive bootstrap scheme

Given the settings of Eq. (1), the confidence bands for the trend were derived by using the following autoregressive wild bootstrap scheme:

1. obtain the estimate of the trend $\hat{m}(t)$ by using the bandwidth \tilde{h} and derive the residuals $\hat{z}_t = X_t - \hat{m}(t)$;
2. derive the bootstrap errors $z_t^* = \xi_t^* \hat{z}_t$, where $\xi_t^* = \gamma \xi_{t-1}^* + v_t^*$, $v_t^* \sim$ i.i.d. $N(0, 1 - \gamma^2)$ and $\gamma = \theta^{1/l}$, with $\theta = 0.1$ and $l = 1.75 \sqrt[3]{n}$; and
3. build the bootstrap series $X_t^* = \hat{m}(t/n) + z_t^*$ for $t = 1, \dots, n$ and estimate the trend $\hat{m}^*(t)$ upon it by using the same bandwidth \tilde{h} used in step 1.

As mentioned, the scheme produces valid confidence bands under the assumption of a trend coupled with an autocorrelated process.

3. Direct estimators of the largest Lyapunov exponent

Let \mathbf{X}_i be a point of the reconstructed trajectory in \mathbb{R}^d . The neighborhood of \mathbf{X}_i within a radius ε is defined as $U(\mathbf{X}_i, \varepsilon) = \{\mathbf{X}_j, j \neq i : \|\mathbf{X}_i - \mathbf{X}_j\| \leq \varepsilon\}$ and its cardinality is denoted as $\text{card}(U(\mathbf{X}_i, \varepsilon))$. We denote with $\Delta_t(\mathbf{X}_i, \varepsilon)$ the average distance between \mathbf{X}_i and its nearest neighbors after t steps ahead in the future,

$$\Delta_t(\mathbf{X}_i, \varepsilon) = \frac{1}{\text{card}(U(\mathbf{X}_i, \varepsilon))} \sum_{\mathbf{X}_j \in U(\mathbf{X}_i, \varepsilon)} \|\mathbf{X}_{i+t} - \mathbf{X}_{j+t}\|.$$

It is expected that $\Delta_t(\mathbf{X}_i, \varepsilon) \approx \exp(\lambda_1 t) \Delta_0(\mathbf{X}_i, \varepsilon)$, where λ_1 is the largest Lyapunov exponent. Hence, for every point \mathbf{X}_i we can monitor the evolution in time of $\Delta_t(\mathbf{X}_i, \varepsilon)$, and we denote with $S(t, \varepsilon)$ its

average (in the log-scale) over the n phase-space points:

$$S(t, \varepsilon) = \frac{1}{n} \sum_{i=1}^n \ln(\Delta_t(\mathbf{X}_i, \varepsilon)). \quad (A2)$$

In the presence of a chaotic dynamics, $S(t, \varepsilon)$ increases linearly with t , and the slope of the linear scaling region is the direct estimator of λ_1 . This should be observable for a reasonable range of radii ε and until the extent of the attractor is reached so that the trajectories fold back. In the initial proposal by Rosenstein *et al.*³⁰ only the nearest neighbor is considered so that $\text{card}(U(\mathbf{X}_i, \varepsilon)) = 1$, whereas Kantz³¹ consider a set of nearest neighbors whose cardinality typically depends upon the sample size, provided that neighbors that are too close in time are discarded as to avoid spurious effects.

4. False nearest neighbors method

The basic idea is monitoring those phase-space points that should not be neighbors but are neighbors just because the dimension of the embedding space is too low. Assume that the minimum embedding dimension for a given time series S_i is d_0 . This means that in an d_0 -dimensional delay space the reconstructed attractor is a one-to-one image of the attractor in the original phase space and its topological properties are preserved. However, if the embedding dimension is $d < d_0$, then the transition from d_0 to d is a projection that no longer preserves the topological structure of the attractor. Therefore, points can become *false neighbors* in a dimensional space $d < d_0$. Hence, for each point in the reconstructed space we take its closest neighbors in d dimensions and calculate the proportion of points whose distances crosses a given threshold when increasing the dimension d .⁸ Such proportion is plotted over d and typically, one chooses a value for the embedding dimension d such that the proportion of false neighbors falls below 10%.

5. Recurrence plot

The importance of the recurrence plot is that the presence of structure can be visualized by means of color graphics. Once the dynamical system is reconstructed by means of delay coordinates, the distance between all pairs of vectors $x(i)$ and $x(j)$ is computed and various color codes are assigned to different distances. For random signals, a uniform distribution of colors over the entire plane is obtained and for deterministic signals we obtain coherent structures in the recurrence plot. In physical terms, it compares the distance distribution between pairs of vectors in the reconstructed state space with the distance distribution between different orbits evolving over time.¹⁸

In a sense, the simple examination of the time series and their recurrence graphs often indicates whether a comprehensive analysis of significant correlation can be performed (more precisely, such an examination often indicates that the analysis should not be performed). Similarly, time series that show rare bursts in otherwise unexplored phase-space regions, as well as non-stationary series and/or the absence of close returns in phase space, are not promising candidates for the search for dissipative low-dimensional chaos.¹⁰¹

6. Space-time separation graph and Theiler window

While the recurrence graph shows absolute times, the space-time separation graph introduced by Provenzale *et al.*¹⁰¹ is integrated along the parallel to the diagonal and, therefore, only shows relative times. Usually, lines of constant probability are drawn per unit of time for points that are an ε -neighbor of the current point, when their temporal distance is δt . This helps to identify the temporal correlation within the time series and is relevant to estimate a reasonable delay time, however, it turns out to be more important to calculate the Theiler W window, which is widely used in dimensional analysis and for the calculation of the Lyapunov exponent. In other words, this graph shows how large the temporal distance between points is so that it can be assumed that they form independent samples according to invariant measurements.¹⁰² This method together with the Theiler window arose from the need to be able to obtain reliable results in the correlation integral.

Theiler¹⁰³ shows that short-term correlations can produce fairly curved lines called *knees* in the correlation integral due to the one-dimensional nature of the trajectory and this produces a bias in the estimate of the dimension. Moreover, the asymptotic results for U -statistics require independence or weak-dependence. For these reasons, the sum in the sample correlation integral contains the points whose temporal distance is greater than some W . The curves of the space-time separation graph can be used to choose a value for W ; in the case of noise from non-stationary power laws the graph indicates that there is no value of W for which the correlation integral reflects global scaling due to recurrence. For chaotic time series, contour curves of the space-time plot initially rise, then oscillate around a constant value, while for series with color noises they continue to rise.¹⁰⁴ An alternative way to estimate the Theiler window is to multiply the autocorrelation time by three.¹⁰⁵

DATA AVAILABILITY

Data sharing is not applicable to this article as no new data were created or analyzed in this study.

REFERENCES

- ¹N. J. Shackleton, M. A. Hall, and E. Vincent, *Paleoceanography* **15**, 565, <https://doi.org/10.1029/2000PA000513> (2000).
- ²N. J. Shackleton, R. Fairbanks, T.-c. Chiu, and F. Parrenin, *Quat. Sci. Rev.* **23**, 1513 (2004).
- ³L. Skinner and H. Elderfield, *Paleoceanography* **22**, PA1205, <https://doi.org/10.1029/2006PA001338> (2007).
- ⁴B. Martrat, J. O. Grimalt, N. J. Shackleton, L. de Abreu, M. A. Hutterli, and T. F. Stocker, *Science* **317**, 502 (2007).
- ⁵T. Blunier and E. J. Brook, *Science* **291**, 109 (2001).
- ⁶G. Mollenhauer, M. Kienast, F. Lamy, H. Meggers, R. R. Schneider, J. M. Hayes, and T. I. Eglinton, *Paleoceanography* **20**, PA1016, <https://doi.org/10.1029/2004PA001103> (2005).
- ⁷M. Ghil, M. Allen, M. Dettinger, K. Ide, D. Kondrashov, M. Mann, A. W. Robertson, A. Saunders, Y. Tian, F. Varadi *et al.*, *Rev. Geophys.* **40**, 3, <https://doi.org/10.1029/2000RG000092> (2002).
- ⁸H. Kantz and T. Schreiber, *Nonlinear Time Series Analysis* (Cambridge University Press, 2004). Vol. 7.
- ⁹H. Abarbanel, *Analysis of Observed Chaotic Data* (Springer Verlag, New York, 1996).
- ¹⁰K.-S. Chan and H. Tong, *Chaos: A Statistical Perspective* (Springer Verlag, New York, 2001).

- ¹¹S. Giannerini and R. Rosa, *Stud. Nonlinear Dyn. Econometrics* **8**(2), 11 (2004).
- ¹²S. Giannerini, in *Handbook of Statistics: Time Series*, Handbook of Statistics, Vol. 30, edited by T. Subba Rao and C. Rao (Elsevier, 2012), pp. 43–63.
- ¹³J. Fan and Q. Yao, *Nonlinear Time Series. Nonparametric and Parametric Methods* (Springer Verlag, New York, 2005), p. xx+551.
- ¹⁴E. Hillebrand, F. Pretis, and T. Proietti, *J. Econom.* **214**, 1 (2020).
- ¹⁵See <http://www.climateeconometrics.org> for more information on econometrics methods applied to climate-economic research.
- ¹⁶*MATLAB R2016a* (The MathWorks Inc., Natick, MA, 2016).
- ¹⁷R Core Team, *R: A Language and Environment for Statistical Computing*, version 3.6.2 patched (2020-01-03 r77629) (R Foundation for Statistical Computing, Vienna, 2020).
- ¹⁸J. Dasan, T. Ramamohan, A. Singh, and P. R. Nott, *Phys. Rev. E* **66**, 021409 (2002).
- ¹⁹I. Choi, *Almost All about Unit Roots: Foundations, Developments, and Applications*, Themes in Modern Econometrics (Cambridge University Press, 2015).
- ²⁰M. Friedrich, S. Smeekes, and J.-P. Urbain, *J. Econom.* **214**, 81 (2020).
- ²¹P. Yiou, E. Baert, and M.-F. Loutre, *Surv. Geophys.* **17**, 619 (1996).
- ²²S. Mallat, *A Wavelet Tour of Signal Processing* (Elsevier, 1999).
- ²³C. Torrence and G. P. Compo, *Bull. Am. Meteorological Soc.* **79**, 61 (1998).
- ²⁴P. Kumar and E. Foufoula-Georgiou, *Wavelets Geophys.* **4**, 1 (1994).
- ²⁵A. Prokoph and F. Barthelmes, *Comput. Geosci.* **22**, 1097 (1996).
- ²⁶A. Berger and M.-F. Loutre, *Quat. Sci. Rev.* **10**, 297 (1991).
- ²⁷G. P. Weedon, *Time-series Analysis and Cyclostratigraphy: Examining Stratigraphic Records of Environmental Cycles* (Cambridge University Press, 2003).
- ²⁸C. Diks, J. Van Houwelingen, F. Takens, and J. DeGoede, *Phys. Lett. A* **201**, 221 (1995).
- ²⁹S. Giannerini, E. Maasoumi, and E. Bee Dagum, *Biometrika* **102**, 661 (2015).
- ³⁰M. Rosenstein, J. Collins, and C. De Luca, *Physica D* **65**, 117 (1993).
- ³¹H. Kantz, *Phys. Lett. A* **185**, 77 (1994).
- ³²S. Giannerini and R. Rosa, *Phys. D Nonlinear Phenom.* **155**, 101 (2001).
- ³³M. Shintani and O. Linton, *J. Econom.* **120**, 1 (2004).
- ³⁴Y. Pesin, *Dimension Theory in Dynamical Systems: Contemporary Views and Applications*, Chicago Lectures in Mathematics (University of Chicago Press, 1997).
- ³⁵C. D. Cutler, *Dimension Estimation and Models*, Nonlinear Time Series, Vol. 1, edited by H. Tong (World Scientific, Singapore, 1993).
- ³⁶P. Grassberger and I. Procaccia, *Phys. Rev. Lett.* **50**, 346 (1983).
- ³⁷C. D. Cutler, “A theory of correlation dimension for stationary time series,” *Phil. Trans. R. Soc. Lond. A* **348**, 343–355 (1994).
- ³⁸S. Borovkova, “Estimation and prediction for nonlinear time series,” Ph.D. thesis, University of Groningen, 1998.
- ³⁹S. Borovkova, R. Burton, and H. Dehling, *Trans. Am. Math. Soc.* **353**, 4261 (2001).
- ⁴⁰S. Borovkova, R. Rosa, and L. Sardonini, *Chaos* **21**, 023124 (2011).
- ⁴¹K.-S. Chan, S. Giannerini, G. Goracci, and H. Tong, “Unit-root test within a threshold ARMA framework,” Tech. Rep., University of Iowa and University of Bologna, 2020.
- ⁴²S. Ng and P. Perron, *Econometrica* **69**, 1519 (2001).
- ⁴³P. Perron and Z. Qu, *Econom. Lett.* **94**, 12 (2007).
- ⁴⁴J. G. De Gooijer *et al.*, *Elements of Nonlinear Time Series Analysis and Forecasting* (Springer, 2017).
- ⁴⁵P. Grassberger and I. Procaccia, *Phys. Rev. A* **28**, 2591 (1983).
- ⁴⁶C. Nicolis and G. Nicolis, *Proc. Natl. Acad. Sci. U.S.A.* **83**, 536 (1986).
- ⁴⁷G. Bond, W. Broecker, S. Johnsen, J. McManus, L. Labeyrie, J. Jouzel, and G. Bonani, *Nature* **365**, 143 (1993).
- ⁴⁸R. Boch, H. Cheng, C. Spötl, R. L. Edwards, X. Wang, and P. Häuselmann, *Clim. Past* **7**, 1247 (2011).
- ⁴⁹G. E. Moseley, C. Spötl, A. Svensson, H. Cheng, S. Brandstätter, and R. L. Edwards, *Geology* **42**, 1043 (2014).
- ⁵⁰M. Luetscher, R. Boch, H. Sodemann, C. Spötl, H. Cheng, R. L. Edwards, S. Frisia, F. Hof, and W. Müller, *Nat. Commun.* **6**, 1 (2015).
- ⁵¹G. E. Moseley, C. Spötl, H. Cheng, R. Boch, A. Min, and R. L. Edwards, *Quat. Sci. Rev.* **127**, 229 (2015).
- ⁵²X. Zeng, R. Pielke, and R. Eykholt, *J. Atmos. Sci.* **49**, 649 (1992).
- ⁵³C. Nicolis and G. Nicolis, *Nature* **311**, 529 (1984).

- ⁵⁴P. Grassberger, *Nature* **323**, 609 (1986).
- ⁵⁵K. Fraedrich, *J. Atmos. Sci.* **44**, 722 (1987).
- ⁵⁶C. L. Keppen and C. Nicolis, *J. Atmos. Sci.* **46**, 2356 (1989).
- ⁵⁷V. Cuculeanu and A. Lupu, *J. Geophys. Res.* **106**, 17961, <https://doi.org/10.1029/2001JD900148> (2001).
- ⁵⁸B. H. Petkov, *Appl. Math. Comput.* **260**, 35 (2015).
- ⁵⁹G. Badin and D. I. Domeisen, *J. Atmos. Sci.* **71**, 1494 (2014).
- ⁶⁰D. Ruelle, *Proc. R. Soc. Lond. A* **427**, 241 (1990).
- ⁶¹A. Tsonis, J. Elsner, and K. Georgakakos, *J. Atmos. Sci.* **50**, 2549 (1993).
- ⁶²N. C. Slowey, G. M. Henderson, and W. B. Curry, *Nature* **383**, 242 (1996).
- ⁶³M. Raymo, *Paleoceanography* **12**, 577, <https://doi.org/10.1029/97PA01169> (1997).
- ⁶⁴A. Aksu, P. Mudie, A. De Vernal, and H. Gillespie, *Palaeogeogr. Palaeoclimatol. Palaeoecol.* **92**, 121 (1992).
- ⁶⁵L. de Abreu, F. F. Abrantes, N. J. Shackleton, P. C. Tzedakis, J. F. McManus, D. W. Oppo, and M. A. Hall, *Paleoceanography* **20**, PA3009, <https://doi.org/10.1029/2004PA001091> (2005).
- ⁶⁶M.-F. Loutre and A. Berger, *Glob. Planet. Change* **36**, 209 (2003).
- ⁶⁷W. S. Broecker and G. M. Henderson, *Paleoceanography* **13**, 352, <https://doi.org/10.1029/98PA00920> (1998).
- ⁶⁸C. Lorius, J. Jouzel, C. Ritz, L. Merlivat, N. Barkov, Y. S. Korotkevich, and V. Kotlyakov, *Nature* **316**, 591 (1985).
- ⁶⁹I. J. Winograd, T. B. Copen, J. M. Landwehr, A. C. Riggs, K. R. Ludwig, B. J. Szabo, P. T. Kolesar, and K. M. Revesz, *Science* **258**, 255 (1992).
- ⁷⁰K. R. Ludwig, K. R. Simmons, B. J. Szabo, I. J. Winograd, J. M. Landwehr, A. C. Riggs, and R. J. Hoffman, *Science* **258**, 284 (1992).
- ⁷¹C. I. Wong and D. O. Breecker, *Quat. Sci. Rev.* **127**, 1 (2015).
- ⁷²G. H. Denton, R. F. Anderson, J. Toggweiler, R. Edwards, J. Schaefer, and A. Putnam, *Science* **328**, 1652 (2010).
- ⁷³R. Drysdale, J. Hellstrom, G. Zanchetta, A. Fallick, M. S. Goñi, I. Couchoud, J. McDonald, R. Maas, G. Lohmann, and I. Isola, *Science* **325**, 1527 (2009).
- ⁷⁴L. Skinner and N. Shackleton, *Quat. Sci. Rev.* **25**, 3312 (2006).
- ⁷⁵B. Martrat, J. O. Grimalt, C. Lopez-Martinez, I. Cacho, F. J. Sierro, J. A. Flores, R. Zahn, M. Canals, J. H. Curtis, and D. A. Hodell, *Science* **306**, 1762 (2004).
- ⁷⁶M. S. Goñi, F. Eynaud, J.-L. Turon, and N. Shackleton, *Earth Planet. Sci. Lett.* **171**, 123 (1999).
- ⁷⁷M. S. Goñi, M.-F. Loutre, M. Crucifix, O. Peyron, L. Santos, J. Duprat, B. Malaizé, J.-L. Turon, and J.-P. Peypouquet, *Earth Planet. Sci. Lett.* **231**, 111 (2005).
- ⁷⁸D. Pailler and E. Bard, *Palaeogeogr. Palaeoclimatol. Palaeoecol.* **181**, 431 (2002).
- ⁷⁹L. E. Lisiecki, *Nat. Geosci.* **3**, 349 (2010).
- ⁸⁰J. Z. Imbrie, A. Imbrie-Moore, and L. E. Lisiecki, *Earth Planet. Sci. Lett.* **307**, 94 (2011).
- ⁸¹D. W. Oppo, L. D. Keigwin, J. F. McManus, and J. L. Cullen, *Paleoceanography* **16**, 280, <https://doi.org/10.1029/2000PA000527> (2001).
- ⁸²D. J. Thomson, *Phil. Trans. R. Soc. Lond. A* **332**, 539 (1990).
- ⁸³L. Keigwin and G. Jones, *J. Geophys. Res.* **99**, 12397, <https://doi.org/10.1029/94JC00525> (1994).
- ⁸⁴W. Dansgaard, S. Johnsen, H. Clausen, D. Dahl-Jensen, N. Gundestrup, C. Hammer, C. Hvidberg, J. Steffensen, A. Sveinbjörnsdóttir, J. Jouzel *et al.*, *Nature* **364**, 218 (1993).
- ⁸⁵P. M. Grootes, M. Stuiver, J. White, S. Johnsen, and J. Jouzel, *Nature* **366**, 552 (1993).
- ⁸⁶D. Meese, A. Gow, R. B. Alley, G. Zielinski, P. Grootes, M. Ram, K. Taylor, P. A. Mayewski, and J. Bolzan, *J. Geophys. Res.* **102**, 26411, <https://doi.org/10.1029/97JC00269> (1997).
- ⁸⁷I. Cacho, J. O. Grimalt, C. Pelejero, M. Canals, F. J. Sierro, J. A. Flores, and N. Shackleton, *Paleoceanography* **14**, 698, <https://doi.org/10.1029/1999PA900044> (1999).
- ⁸⁸W. S. Broecker, *Nature* **372**, 421 (1994).
- ⁸⁹J. D. Cox, *Climate Crash* (Joseph Henry Press, Washington, DC, 2005).
- ⁹⁰D. V. Alexandrov, I. A. Bashkirtseva, and L. B. Ryashko, *Eur. Phys. J. B* **88**, 304 (2015).
- ⁹¹J. Weertman, *Nature* **261**, 17 (1976).
- ⁹²D. Alexandrov, I. Bashkirtseva, and L. Ryashko, *Physica D* **343**, 28 (2017).
- ⁹³D. V. Alexandrov, I. A. Bashkirtseva, S. P. Fedotov, and L. B. Ryashko, *Eur. Phys. J. B* **87**, 227 (2014).
- ⁹⁴B. Saltzman, *Advances in Geophysics* (Elsevier, 1978), pp. 183–304, Vol. 20.
- ⁹⁵B. Saltzman and R. E. Moritz, *Tellus* **32**, 93 (1980).
- ⁹⁶B. Saltzman, A. Sutera, and A. Evenson, *J. Atmos. Sci.* **38**, 494 (1981).
- ⁹⁷B. Saltzman, *Tellus* **34**, 97 (1982).
- ⁹⁸B. Saltzman and A. Sutera, *J. Atmos. Sci.* **41**, 736 (1984).
- ⁹⁹L. A. Smith, C. Ziehmann, and K. Fraedrich, *Q. J. R. Meteorol. Soc.* **125**, 2855 (1999).
- ¹⁰⁰M. Cencini, F. Cecconi, and A. Vulpiani, *Chaos: From Simple Models to Complex Systems* (World Scientific, 2009).
- ¹⁰¹A. Provenzale, L. A. Smith, R. Vio, and G. Murante, *Physica D* **58**, 31 (1992).
- ¹⁰²R. Hegger, H. Kantz, and T. Schreiber, *Chaos* **9**, 413 (1999).
- ¹⁰³J. Theiler, *Phys. Rev. A* **34**, 2427 (1986).
- ¹⁰⁴S. J. Guastello and R. A. Gregson, *Nonlinear Dynamical Systems Analysis for the Behavioral Sciences Using Real Data* (CRC Press, 2016).
- ¹⁰⁵R. A. Heath, *Nonlinear Dynamics: Techniques and Applications in Psychology* (Psychology Press, 2014).